Performance Assessment of a Newly Constructed Skewed Half-Through Railway Bridge through Integrated Sensing

Weiwei Lin[1], Liam J. Butler[2,3], Mohammed Z.E.B. Elshafie[4], and Campbell R. Middleton[5]

[1]Associate Professor, Ph.D., A.M.ASCE, Dept. of Civil and Environmental Engineering,Waseda Univ., Shinjuku-ku, Tokyo 169-8555, Japan (corresponding author). E-mail: linweiwei@aoni.waseda.jp

[2]Research Associate, Ph.D., PEng., Department of Engineering, University of Cambridge, Trumpington Street, Cambridge, CB2 1PZ, United Kingdom. E-mail: lb643@cam.ac.uk

[3]Group Leader, Ph.D., PEng., Lloyd's Registration Foundation Programme on Data-Centric Engineering, The Alan Turing Institute, NW1 2DB, United Kingdom

[4]Lecturer, Ph.D., M.ASCE, Department of Engineering, University of Cambridge, Trumpington Street, Cambridge, CB2 1PZ, United Kingdom. E-mail: me254@cam.ac.uk

[5]Professor, D.I.C., Ph.D., CEng., CPEng., FICE., MIE(Aust)., Department of Engineering, University of Cambridge, Trumpington Street, Cambridge, CB2 1PZ, United Kingdom. E-mail: crm11@cam.ac.uk

Abstract

Half-through steel plate girder bridges are widely used across the U.K.'s railway network. However, very few studies have investigated their real in-service behaviour. Concurrently, the use of advanced sensor systems, such as those utilizing fibre-optic sensors, have begun to find widespread use in structural health monitoring due to their high accuracy and long-term stability and durability. In this paper, the real performance of a newly constructed skewed half-through plate girder railway-bridge was assessed through the use of an integrated fiber optic monitoring system installed during the bridges' construction. Monitoring data recorded during the passage of 12 separate trains consisted of strains measured along the lengths of the main steel plate girders and cross beams. On the basis of available design and construction information, a 3-D finite element model capable of simulating the railway bridge's response was constructed and used to investigate and provide comparisons with monitoring results of the performance of such bridges under passing trains. The influence of track cant on load distribution between the two main girders was discussed, and the live load utilisation percentage of the main girders was estimated to be approximately 37% of its design capacity. In addition, the effect of different transverse cross beam end-connection details (pinned or moment connected) and the influence of axle load distribution through track ballast on the overall

response of the bridge structure were evaluated. The results obtained in this study have not only led to the establishment of a comprehensive performance baseline for the newly constructed bridge for long-term condition monitoring, but also may be used for improving both the design and in-service structural evaluation of such bridges.

Key Words:Half through railway bridge; structural health monitoring; fibre optic sensors; numerical analysis; performance assessment.

Introduction

Plate girder bridges consisting of two main longitudinal girders, multiple transverse cross-girders, and a composite reinforced concrete deck are widely used in bridge structures because they provide an economical design and rapid form of constructions. This form of bridge became popular in the late 1800's for the construction of railroad bridges (Kopare and Upase, 2015). Plate girder bridges typically consist of either a full depth beam type or a half through type (Fig.1), depending on minimum clearance requirements. A half-through bridge configuration is widely used in railway bridges where available clearance between the rail surface and the clearance beneath the bridge is too shallow to accommodate the full depth of the structural elements spanning between the bridge supports. In addition, it is sometimes not possible to arrange a bridge span square to the feature that it crosses, particularly where it is important to maintain a relatively straight alignment of a roadway or rail line above or below the bridge; in these cases a skewed configuration is required. This skewed arrangement increases the span length and gives rise to additional torsional effects resulting in relatively complex support reactions. For continuous composite bridges with span lengths of up to approximately 200ft (61 m), plate girder bridges represent the majority of the bridge population (Knight, 1983).

In recent years, research on both straight and skewed plate girder bridges has been performed. In 2002, Sakurai et al. reported their studies on two plate-girder skew bridges based on numerical analysis techniques, focusing on the effects of skew and bending at piers. Quadrato et al. (2010) presented their findings of an investigation of the connection details and bracing layouts for stability bracing of skewed steel plate girder bridges. The results indicated that the use of split pipe stiffeners (allowing perpendicular connections to the cross-frame connection tab) provided a stiffer connection between the cross-frame and the girder while increasing its torsional stiffness. Kaliyaperumal et al. (2011) presented advanced modelling techniques for steel plate girder railway bridges where eigenvalue analyses and time history dynamic analyses were carried out. The results demonstrated that a full bridge model

using a combination of beam and shell elements could provide a reasonably accurate and computationally efficient way of capturing the dynamic behavior of the bridge. Zhou et al. (2016) investigated the effects of cross-frame layout on lateral flange bending stresses in skewed steel plate girder bridges. The findings of this study showed that cross frames placed parallel to the angle of skew (Fig.2 (a)) produced significantly lower lateral flange bending stresses compared with cases in which cross frames were staggered and placed perpendicular to the girder line (Fig.2 (c)). Hendy and Jones (2016) investigated buckling cases for half-through plate girder bridges where the effective length for buckling is shorter than the half wavelength for buckling and demonstrated that the series of correction curves used in BS 5400-3 (2000) were unnecessary. Different from previous studies, this research aims to investigate the actual in-service behavior of such bridges by using both modern sensing technologies and finite element modelling.

Despite previous studies on half-through plate girder bridges, the actual in-service performance of such bridges (e.g. the effect of end connections of cross beams, the influence of track cant and axle load distribution scenarios etc.) has not yet been investigated. With the development of robust fibre optic (FOS) sensing technologies, these systems are being used increasingly worldwide for assessing and better understanding the in-service performance of bridges. FOS techniques offer several distinct advantages over traditional electrical-based strain sensors, such as having greater accuracy, reduced wiring requirements, and being non-corrosive nature and electromagnetically inert. Recently, FOS has been used in structural monitoring under static and dynamic in-service conditions (Regier and Hoult, 2014; Scarella et al., 2016; Webb et al., 2017), for fatigue assessment (Wijesinghe et al., 2013), and for measuring scour (Zarafshan et al., 2012; Kong et al., 2017) in bridge structures.

This paper provides an analysis of data obtained from a newly constructed 'self-sensing' skewed half-through railway bridge instrumented with an advanced network of fibre-optic sensors. The primary contributions of this study include: (1) testing and demonstrating the effectiveness of the integrated sensing system for capturing the response of the bridge superstructure elements under passing trains; (2) constructing and validating a 3D linear finite element model of a skewed half-through bridge using data obtained from the sensor network; (3) evaluating the effect of variations in load distribution and the cross-beam end connection details on the bridge's response; and (4) assessing the live load utilisation percentage of the primary structural elements by comparing information gathered from the monitoring data, the validated FE model predictions and Eurocode design equations. To the best of the authors' knowledge, this study represents the first time in which such an extensive and advanced fibre-optic based monitoring system has been used to quantify and assess the in-service performance of a skewed half-through railway bridge. This sensing capability is leveraged through detailed data and numerical analyses in order to investigate the actual effects of critical design factors (such as loading condition caused by eccentricity, centrifugal forces etc.) on the

behavior and the real in-service performance of structural members (i.e. main plate girders and cross beams).

Description of the Instrumented Bridge

The bridge evaluated in this study is referred to as Intersection Bridge 20A and is located along the West Coast Main (railway) Line, in Staffordshire, United Kingdom. This bridge represents an important structure in a large rail upgrade and redevelopment project known as the Stafford Area Improvements Programme completed in 2016. The bridge was designed as a Network Rail 'E-type' steel half-through bridge with a single skew span of 26.84m, supported on four bearings on reinforced concrete abutments (Butler et al., 2016, Butler et al., 2018). The width of the bridge cross-section (distance between the webs of the twin main girders) was 7.3m. The bridge carries two new rail lines on ballasted track over another existing heavily trafficked rail line. Design details of the cross-section are shown in Fig.3.

To achieve minimum structural depth requirements, a composite beam and slab arrangement was adopted for the bridge deck. The superstructure consists of a pair of main longitudinal steel I-girders and a composite deck supported on secondary steel cross girders. In the design, web stiffeners were used to increase stability and avoid local buckling of the main girder top flanges and also to prevent web buckling. Additional flange plates (doubler plates) were used in the region of greatest moment near the mid-span. Two different flange thicknesses of 60 mm and 120 mm were used for the girder end section and the mid-span sections (i.e. doubler plates), respectively. Transverse cross beams, with alternating pinned and moment connections, were spaced at every 1.5 meters. To provide lateral buckling restraint to the top flanges, U-frames consisting of vertical web stiffeners were used on the main girders at locations corresponding to moment-connected cross beams locations. Typical cross beam arrangements in skewed half through railway bridges are depicted in Fig.2.

The cross beams supporting the concrete deck were arranged orthogonal to the main girders in the centre region of the bridge and were arranged in a fanned pattern near both ends of the bridge. Fig.4 presents the plan view of the bridge superstructure. Glass fiber reinforced polymer (GFRP) panels were placed between adjacent cross girders (without using any bonding materials) as permanent formwork for concrete deck casting, as shown in Fig.5. Composite action between the concrete slab and steel cross beams was accomplished using a double row of shear stud connectors welded along the top flange of the transverse cross beams. Construction of the bridges' piled foundations started in December 2014 and the bridge was opened to commercial rail traffic in April 2016. The west elevation and top view of the completed bridge are shown in Fig.6.

Monitoring Programme and Sensor System

Using the integrated fibre optic monitoring system, strain measurements were taken in order to investigate the mechanical performance of the bridge under normal operating conditions. The strain variations of the instrumented main girders and cross beams under twelve live trains were measured. The monitoring of the bridge in-service was undertaken under live trains as shown in Fig.7.

Sensor System

Fibre optic strain sensors (FOS) based on fibre Bragg gratings (FBGs) were installed on the bridge during its construction (refer to Butler et al., 2018 for further details). The FBGs used in this study were written in low bend loss fibre and contained sensor arrays with up to 20 individual FBGs spaced at one meter. They were produced with a glass-fibre reinforced polymer coating in order to provide adequate robustness and durability during installation and operation. Field monitoring data was captured using a 4-channel fibre-optic interrogator produced by Micron Optics (sm130-700) in combination with a Micron Optics Channel Multiplexer (sm041) which allows the system to simultaneously interrogate a total of 16 channels (with up to 20 FBGs per channel) at a sampling frequency of 250 Hz. Measurements from a total of 108 FBG strain and temperature sensors installed on the main girders, cross beams, and within the concrete deck are reported as part of this study. In order to convert the change in wavelength measured using the FBG sensors to a change in strain ($\Delta\varepsilon_m$), Eq. (1) was used,

$$\Delta\,\varepsilon_m = \frac{1}{k_\varepsilon}\left[\frac{\Delta\lambda}{\lambda_0}\right] \tag{1}$$

where the optical coefficient k_ε = 0.78 and $\Delta\lambda/\lambda_0$ is the relative change in wavelength (Kreuzer, 2006). Note that FBG sensors are also highly sensitive to temperature changes however, it was assumed that during the passage of a train no significant change in ambient temperature was experienced. Eighty FBG strain sensors in total (20 sensors per array) were installed along the top and bottom flanges of both main girders. A total of 28 strain FBG sensors (7 sensors per array) were installed along both top and bottom flanges of two adjacent mid-span cross beams (one pin-connected and one moment-connected) and one skewed cross beam at the bridge end, as shown in Fig.4. Some of the sensors installed on the main girders and middle cross beams of the bridge are shown in Fig.8.

Train Types

The primary rail loading passing over the bridge consists of two typical U.K. train types including the London

Midland Class 350 Desiro (Type-1) and the Cross Country Class 221 Super Voyager (Type-2). Schematic drawings of both train types, which include axle spacing and axle weights are given in Fig.9. These axle weights are referred to as unladen axle loads, since no live load from passengers is included. Based on these schematics, the axle weights of train Type-2 are significantly larger than those of train Type-1. A total of 12 trains and their associated strain responses were recorded during this study. Train speeds were determined using the dynamic strain data (captured at 250 Hz) and by considering the axle spacing and bridge length. Video recordings of each train were also captured and used to verify the calculated speeds. Note that the bridge carries two lines of rail traffic and therefore, each recorded train has been designated as either travelling along the west or east track. Train speeds varied between 117 km/h and 162 km/h, with an average speed of 143 km/h. Table 1 summarizes the various train numbers and their associated types, direction of travel, and speed.

In the live train tests, passengers were present in trains in the in-service condition; however, the ratio of passenger live load to train self-weight is not available since no data on the number of passengers in different trains was available. According to the design information, the average ratio of crush laden axle load (represents an extreme form of passenger loading or a train with serious capacity limitations) to unladen axle load of the London Midland Class 350 Desiro (train Type-1) is approximately 1.25, which is used as the maximum possible train load in real in-service condition for this train type. By assuming that the in-service passenger load is relatively small compared to the train self-weight (and the crush axle laden design axle load), the unladen axle load was used in the numerical analyses to compare with the measured results, while the crush laden axle (design) load is used to assess the utilisation of the bridge under service conditions.

Numerical Modeling

Model Building

The modeling of the bridge was carried out in three dimensions using the finite-element software *TNO DIANA*. Solid elements (eight nodes, three degrees of freedom per node) were used to simulate the concrete slab, and shell elements (four nodes, five degrees of freedom per node) were used to model the steel I-girders, cross beams, and stiffeners, as shown in Fig.10. Rebar elements (two nodes, with one degree of freedom at each node) were used for modeling the reinforcing bars in the concrete slab. In the numerical modeling, the mesh generation (or element size) was constrained appropriately to avoid large aspect ratios (<2.0, in this study). The mesh quality was tested to ensure that no element deviated significantly from its theoretically ideal element size. The mesh quality tests included investigating element angles, aspect ratios, positioning of the mid-side node for higher order elements and the extent

of warping.

As the composite section was designed as a full connection via a double layer of shear studs, a complete connection (perfect shear transfer) was assumed at the steel-concrete interface and was modeled by using 8-noded interface elements assigned with very large stiffness. To simplify the model geometry, fully-fixed end connections were assumed when modeling the transverse cross beams connected to the main girder webs. Ancillary structures such as steel access walkways, ballast and prestressed concrete sleepers were not modelled explicitly in the numerical simulation. Concentrated moving loads were applied to simulate the instantaneous position of the moving axle loads of a train. In order to avoid imposing stress concentrations on the concrete deck, the concentrated loads were applied along rail tracks which were modeled using beam elements (two nodes, with six degrees of freedom at each node). As the neutral axis of the total transverse section of the bridge was within the depth of the concrete deck, the contribution of the rail track stiffness to the bridge's flexural stiffness was assumed to be negligible, which is further demonstrated and discussed in the following sections. Rocker-type bearings were used on the real structure and thus pinned and roller boundary connections were assumed when modeling the bridge supports. As previously mentioned, GFRP panels were used as permanent formwork for casting of the reinforced concrete deck. The panels were laid between adjacent cross beams without the use of any adhesive or mechanical connectors. Therefore, GFRP plates were assumed to have no significant contribution to the linear-elastic response of the structure and were therefore not included in the model. A similar modeling method has been employed in several previous studies by the authors (Lin et al, 2013, 2014, 2015, 2017a and 2017b) and will be validated by comparing the numerical predictions with the in-service monitoring results obtained from this bridge.

Material Properties

As the purpose of this study was to investigate the structural performance of the under service condition, material properties of all structural members were considered as ideally elastic. The material properties assigned to the various structural elements were based on actual measured or specified properties used within the constructed bridge. Material tests were performed on the deck concrete and the average 28 day compressive strength of the concrete was 47.1 MPa (equivalent cylinder strength). Materials test results for the compressive strength (and elastic modulus) of the bridge deck concrete on the day of the field monitoring were not available, and therefore, the elastic modulus of concrete was estimated using the 28 day concrete compressive strength. Given that the concrete deck slab is located at a depth which is relatively close to the neutral axis depth of the half-through bridge section, it was assumed that the elastic modulus of concrete will have little effect on the overall elastic response of the bridge under

live loads. Based on the measured compressive strength, a calculated elastic modulus of concrete of 35.0 GPa (determined according to the Eurocode and Eq. (1), where f_{cm} denotes the mean compressive strength of concrete in MPa) and the Poisson's ratio of 0.2 were used in the numerical model. The structural steel was assigned to a nominal yield strength of 355 MPa and a nominal ultimate tensile strength of 490 MPa for the main girders, cross beams and stiffeners. Steel reinforcing bars within the concrete bridge deck were assigned a nominal yield strength of 500 MPa and a nominal ultimate tensile strength of 540 MPa. Perfect bond with no slip between the reinforcing bars and the surrounding concrete was assumed.

$$E_c = 22[f_{cm}/10]^{0.3}\ \text{GPa} \quad (1)$$

Modeling of Transient Loading

According to Eurocode 1 (BS EN 1991-2:2003, Clause 6.4.4), for a simply supported bridge with a span shorter than 40 m and with a design train speed of less than or equal to 200km/h, a dynamic analysis is not required if it's first natural bending frequency is within specified limits which are governed by impact criteria. For the bridge in this study, the span length is 26.8 m, the design train speed is 160 km/h (<200 km/h) and its first natural bending frequency was calculated to be well within the aforementioned limits specified in Eurocode 1. Therefore, a dynamic analysis is not required for the target bridge according to Eurocode 1. Instead, the transient axle loads were applied statically as moving concentrated loads. In the numerical analyses, successive moving loads considering distance between axle loads were applied along the railway tracks to simulate axle loads of the live trains traveling over the bridge. The numerical results (e.g. strain) were taken for each corresponding train location, and the timing data can be determined according to the train moving distance and the train speed. The applied static loads were based on the unladen axle loads (self-weight of vehicles without passengers, goods or other items) provided in Fig.9 and were applied directly on the bridge deck surface along the locations of the rail track. In order to accommodate track alignment and track curvature, ballasted track is often provided with vertical cant between each rail to limit the horizontal forces imposed on the rail. This condition induces both horizontal loading and a transverse moment. To account for this in the numerical analysis, the train live load was distributed along two tracks, in which the loading distribution ratio between the tracks was calculated in order to create a moment equivalent to that induced from a centrifugal force acting at 1.8 m above the track surface. To further simplify the numerical modeling, both vertical (Q_v) and horizontal forces (Q_h) acting on the canted ballasted track (Fig.11(a)) were resolved into a pair of equivalent concentrated vertical forces (Q_1 and Q_2) and horizontal ($Q_h/2$) forces which were applied as concentrated loads directly to the bridge deck as depicted in Fig.11(b).

The actual cant (u) of the completed ballasted track is 100mm. The centrifugal force is taken to act outwards in a horizontal direction at a height (h) of 1.8 m above the running surface and the average thicknesses of the sleeper and ballast were taken as 200 mm and 350 mm, respectively. The horizontal loads (Q_h) arising from centrifugal forces were calculated using Eq. (2):

$$Q_h = \frac{V^2}{127r} Q_v \tag{2}$$

where r is the radius of track curvature (=1600 m in this study) and $V$is the train speed in km/h.

Results and Discussion

Effect of Transient Load Distribution through Ballast

Railway track ballast forms the track bed upon and carries the sleepers on it. It is used to carry and disperse the load from the sleepers and to facilitate drainage of water. In the numerical analyses undertaken, there is some debate over whether or not the track ballast system should be considered in the numerical simulation. To investigate how the assumed loading distribution affects the predicted mechanical behavior of the bridge, both simplified concentrated load model (the one used in this study) and fully considered distributed load model were implemented in the FE model and the resulting responses were also compared to the FBG measured responses.

As shown in Fig.12, two loading distributions were investigated and compared within the FE model. In both loading scenarios, transverse loading due to the centrifugal forces described previously were also considered. When applying the concentrated loads in the FE model, they were applied directly along the rail track which was supported directly on the concrete deck slab. In terms of distributed load, the applied axle loads were distributed across the entire length of the sleeper and projected onto the concrete deck slab at the underside of the ballast; the loading was not applied along the modeled rail track in this case. In this study, the ballast depth above the top of the concrete slab varied between approximately 300 and 400 mm, with an averaged depth of 350 mm used in numerical analyses for the purposes of calculating the load distribution through ballast. As recommended in the Eurocode (EN 1991-2, 2003), load distribution through ballast can be represented by a depth of ballast to width ratio of 4:1, defined as the angle of stress distribution which is applied both longitudinal and transverse to the sleeper (Fig.12(b)).

The associated axle loading and spacing from Train type 1 (refer to Fig.9) was applied within the FE model along the western track in order to investigate the relative effects of both strain distribution scenarios on the main girders and the cross beams. As for the axle load locations, wheel set-2 of Car-2 and wheel set-1 of Car-3 in Fig.9(a) were applied symmetrically about mid-span of the west main girder. When subjected to the concentrated loading (denoted

by the suffix "-PL") scenario, the strain distribution along the west main girder top flange (WMGT-PL), west main girder bottom flange (WMGB-PL), east main girder top flange (EMGT-PL) and east main girder bottom flange (EMGB-PL) were summarized for train no. 3 and 4 (Type-1) as shown in Fig.13 (a). Similarly, the strain distribution on the main girders considering the distributed loading scenario was also included in Fig.13(a) (the suffix "-DL" refers to the distributed load scenario). In addition, the strain distributions on the bottom flange of the middle cross beam (midspan cross-beam with moment end connections) under both concentrated load and distributed load scenarios were compared in Fig.13 (b). The results indicate that the cross beam strain responses predicted by both loading scenarios were very similar (i.e. within 4%). The FE-predicted strain response for both the main girders and the cross beams also closely matched the FBG measured response. Therefore, it can be concluded that the simplified concentrated loading model can be used to evaluate the performance of both main girders and cross beams while having a negligible effect on the predicted results. Subsequent FE results presented are based on the responses derived based on the concentrated loading model.

Main Girder Strain Distribution, Load Sharing, and Live Load Utilisation

As described above, 80 FBG sensors (20 FBG sensors per array) were installed along the top and bottom flanges of both main girders. To investigate the strain variation of the main girders, the strains at the mid-span section of the bridge were compared with the FEM strains generated due to the applied transient loading. For the purpose of investigating the load distribution between the main girders, the strain variation on top and bottom flanges (refer to Figs.14 to 17) of both main girders were reported. Due to the significantly lower train speed for train No.5, the results from Train No.5 were not included in Fig.16. Because of the inconsistent train speeds and different number of train cars, the strain results from train No.9 only is provided as an example in Fig.17.

The strain variation of the top and bottom flanges of the main girders when the London Midland Class 350 Desiro trains (train Type-1) passed over the bridge is shown in Fig.14. The longitudinal strain increases gradually (until $\varepsilon \approx 20\mu\varepsilon$) as wheelset-1 of car-1 (Fig.9 (a)) crosses the mid-span of the bridge. Considering the relatively short car length (20.4 m) and wheelset spacing (14.17 m) compared with the bridge span length (26.84 m), wheelset-2 of car-1 (and wheelset-1 of car-2) is still being supported by the bridge at the time when wheelset-1 of car-1 passes over the bridge. This superposition of consecutive wheelset loads causes an additional increase in strain response at the mid-span prior to a decrease in strain. The peak strain increased to 32 με when the intermediate point of wheelset-2 of car-1 and wheelset-1 of car-2 was located at approximately the mid-span of the bridge. The strain then decreased from 32 με to 18 με before increasing once more when the remaining wheelsets pass over the mid-span fiber optic

sensors. Similar behavior was observed in all sensors on the main girders, indicating that the strain response of the main girders reflects the global behavior of the bridge.

The measured time versus strain measurements were also compared with the FE model results. The comparison indicates that the numerical results predict a similar loading versus time history but predict slightly larger strain values on the top flanges (similar for all trains recorded). Even though unladen axle loads were implemented within the numerical analysis, the strain response predicted by the numerical analysis was still slightly larger compared with the FOS measured results. This comparison suggests that the actual bridge stiffness under service conditions is larger than that predicted by the FE model. This is presumably because of the neglected contribution of bridge accessories in the numerical analyses. In bridge design, the accessory structural members (e.g., handrail and walkway shown in Fig.6 (b)) are generally ignored, but they can contribute to the bridge stiffness in service condition, which was similar to what had been found in a previous study (Lin et al, 2015). Therefore, it can be concluded that the current bridge design method for plate girder bridges is relatively conservative and well within the required safety margin in terms of the flexural strain. In terms of structural health evaluation or assessment for such bridges, however, the contribution of bridge accessories should be taken into account if a closer prediction of behavior is to be obtained.

Another interesting observation relates to the load distribution between the two main girders. For twin girder bridges, the load distribution between the two main girders is critically important for both bridge serviceability (e.g., to limit deflection) and for providing realistic estimates of remaining fatigue life that closely related to in-service stress levels. The load distribution between the two main girders can be determined according to the maximum normal strain on the two main girders, which is summarized in Table 2. For the sake of discussion, ε_{lgt}, ε_{lgb}, ε_{ulgt} and ε_{ulgb} denote strains on the top flange of the loaded main girder, bottom flange of the loaded main girder, top flange of the unloaded main girder, and bottom flange of the unloaded main girder, respectively. The ratios of $\varepsilon_{ulgt}/\varepsilon_{lgt}$ and $\varepsilon_{ulgb}/\varepsilon_{lgb}$ represent the load distribution ratio between unloaded and loaded main girders. When trains passed on the track near the east girder side, the average ratios of $\varepsilon_{ulgt}/\varepsilon_{lgt}$ and $\varepsilon_{ulgb}/\varepsilon_{lgb}$ were 0.46 and 0.57, respectively. When trains passed on the track near the west girder side, however, the average ratios of $\varepsilon_{ulgt}/\varepsilon_{lgt}$ and $\varepsilon_{ulgb}/\varepsilon_{lgb}$decreased to 0.39 and 0.29, respectively. These results indicate that the load distribution factor for the west main girder is much larger than that of the east main girder; that is, the west main girder is consistently carrying a larger portion of the live loading as compared with the east main girder. Considering the similar structural system and live train loads when trains traveled either near the east or west main girder side, the load distribution difference is assumed to be caused by the eccentricity and centrifugal forces due to the curved rail track and track cant. This difference in load distribution between the two main girders also highlights the importance of considering

331 the effects of cant and track curvature in railway bridge design and in-service evaluation.

332 The design live loading for the bridge is based on Load Model 71 (LM71) specified in BS EN 1991-2:1993, as
333 shown in Fig.18. In order to assess the percentage utilisation of the main girders due to live loading, the maximum
334 compressive strain on the top flange and maximum tensile strain on the bottom flange of the main girders under 12
335 live trains are summarized and illustrated in Fig.19. By applying LM71 in the numerical model, the maximum
336 compressive and tensile strains under design live load (i.e. design strains) were determined to be -185 με and 166
337 με, respectively. Based on the monitoring data, a maximum compressive strain response of -55 με was measured
338 during the passage of train No.10, which was approximately 30% of the design strain. As discussed previously, the
339 average ratio of crush laden axle load to unladen axle load is approximately 1.25. Multiplying the maximum
340 recorded strain response (i.e., -55 με) by 1.25 represents an upper bound estimate of the maximum strain response.
341 Therefore, the resulting upper bound on the live load utilisation percentage of the main girder will be approximately
342 37% under crush laden axle load (train with maximum possible number of passengers). Likewise, the maximum
343 tensile strain of 48 με recorded for train No.10 represents a live load utilisation percentage of approximately 29%
344 (upper bound of 36% for crush laden axle load). Therefore, by considering the maximum recorded strains within
345 the top and bottom flanges, when a single train passes over the bridge (for all trains considered in this study), the
346 maximum (upper bound value) percentage utilisation of the main girders is approximately 37% of their intended
347 design loading and well within safe operating conditions.
348
349 ***Cross Beam Strain Response***
350 As discussed previously, sensors were installed along the top and bottom flanges of two adjacent cross beams
351 located near the centre of the bridge span. Both of the instrumented cross beams had different end connection details
352 with one being a pinned (6-bolt end plate) connection and the other a moment (10-bolt stiffened extended end plate)
353 connection (refer to Fig.8(b)). This section evaluates the strain response of the cross beam with moment end
354 connections and a comparison between both cross beam end connection types is provided in the following section.
355 Based on the strain measurements, the neutral axis of the cross beam (moment end connections) when acting fully
356 compositely with the concrete deck slab was found to be located near the top flange of the steel cross beam, thus
357 the measured strains at those sensors were relatively small (i.e. < 5 με). Therefore, only strain variation along the
358 bottom flange of the cross beam has been reported herein. Due to the location of the railway tracks relative to the
359 FBG sensors on the cross beam below, the maximum strain does not occur at the midspan of the cross beam. Instead,
360 it occurs east of the midspan for trains passing on the east track and west of the midspan when trains are passing on

361 the west track. For this reason, the results for sensors located east of midspan (CB-3 in Fig.4)and west of midspan
362 (CB-5), were reported to investigate the strain variation under trains passing over the east and west track,
363 respectively. The numerically derived predicted strains at the corresponding sensor locations were also compared
364 with the measured results.

365 When trains No.1 and 2 passed over the bridge, the strain variation with time at CB-3 on the bottom flange of the
366 middle cross beam is shown in Fig.20 (a). When each wheelset passes over the middle cross beam, the strain at CB-
367 3 increases as a wheelset approaches and decreases as a wheelset moves away from the measured section. Unlike
368 the observed strain response of the main girders, the distinct peaks corresponding to individual wheelset (or bogies)
369 can be identified within the cross beam strain response.

370 The numerically derived predictions are also provided in Fig.20(a). The speeds of the two trains were 147 km/h
371 and 150 km/h respectively, and an average speed of 148 km/h was assumed in moving load analysis in the FE
372 model. The comparison in Fig.20 (a) shows that the numerical results agree well with the actual measurements
373 except some peak strain points, in both magnitude and frequency of the strain response. Similar results were also
374 confirmed for other trains as shown in Fig.20 (b) and Fig.21. Based on the FE-predicted strains and confirmed by
375 the measurement results, the axle loads are more globally distributed along the longitudinal main giders whereas,
376 the cross beams experience a more localised strain response. Though beyond the scope of this current study, the
377 sensing system was able to capture this localised strain response with a high level of detail, which could be used as
378 a monitoring tool for characterising the fatigue characteristics of the cross beams and their end connections.

379

380 ***Effect of Connection Conditions at Cross Beam Ends***

381 As described previously, the cross beams on the bridge are connected to the webs of the main girders with pinned
382 (6-bolt end plate) and moment (10-bolt stiffened extended end plate) connections used alternatively. Although
383 pinned and moment connections were assumed for each respectively in the design as shown in Fig.22, their actual
384 performance in real service is still unknown. To investigate the effect of end connection details on the dynamic
385 strain distribution along the cross beams, the measured response of both moment and pinned cross beams, under
386 passing trains were evaluated and compared.

387 During monitoring, strain on both pinned and moment-connected cross beams was measured only for trains No.1
388 and No.3 (Train Type-1). When train no.1 passed on the east track, the maximum strain occurred at FBG CB-3. The
389 strain variation at FBG CB-3 at the adjacent pinned and moment connections in the mid-span is illustrated in Fig.23
390 (a). Similar strain variations (both magnitude and distribution) were observed in both cross beams with pinned and

391 moment connections. Similar results were also confirmed in the measured strains under train No.3, as indicated in
392 Fig.23(b). By also considering the results shown in Figs.19~20, it can be concluded that the cross beam with pinned
393 end connections behaved similarly to the cross beam with moment end connections. This may be the result of the
394 compositely-connected concrete slab which acts to redistribute the live loading between adjacent cross beams. From
395 the design details shown in Fig.22 and results shown in Fig.23, it may be inferred that the bolted connection of the
396 pinned cross beams may be considered as semi-rigid and provide a certain amount of fixity and moment resistance.
397 By also considering the comparisons in Figs.20 and 21, it may be concluded that modeling pinned connections as
398 moment (fully-fixed) connections had no significant effect on the FE results. Providing more accurate estimates
399 through experimental testing, finite element modeling and in-situ sensing of the real connection ratio (i.e. joint
400 fixity) at the transverse girder end connections is an area requiring further investigation and research.
401
402 **Conclusions**
403
404 A structural monitoring system consisting of a network of 108 FBG fibre optic sensors was designed and installed
405 to investigate the performance of a newly constructed skewed half-through railway bridge during its first several
406 months in-service. Detailed strain variations on both the main girders and cross beams were recorded from field
407 measurements during the passage of 12 passenger trains. A three-dimensional FE model was then constructed to
408 simulate the response of the bridge under representative live loading specified according to Eurocode 1. Based on
409 the presented results, the following conclusions were drawn:
410 (1) The effect of transient load distribution through ballasted track was investigated for the purposes of simplifying
411 the FE model. Concentrated and distributed (area) load distribution scenarios were implemented within the FE
412 model and their corresponding effect on the strain response of the main girders and cross beams were compared.
413 It was found that both load distribution models resulted in very similar predicted responses and the simplified
414 concentrated loading could therefore be used for predicting the structural behavior of the railway bridge.
415 (2) Both the strain response of and load sharing between the two main girders were evaluated using the FBG
416 measured strains recorded for all 12 monitored train passage events. Based on the calculated relative strain
417 percentages of each girder, significant differences in load sharing between the two main girders were
418 confirmed. This is believed to be the result of the complex load distribution path through the ballasted track
419 and the additional lateral loading arising from centrifugal forces caused by track curvature and cant.
420 (3) The strain variations alongthe main girders were compared with the numerical prediction results. The

comparison suggests that that secondary bridge accessories such as access walkways and handrails may contribute significantly to the in-service bridge stiffness. The live load utilisation percentage of the main girders in-service was also evaluated, and the results indicate that the bridge structural capacity is currently only 37% utilised and the bridge is operating well within the in-service safety limits.

(4) A three-dimensional FE model was built to investigate the behavior of the skewed half-through plate girder bridge. The FE-predicted strain variations along both the main girders andcross beams due to live trains agreed well with the actual measured results, demonstrating the validity of the proposed FE model.

(5) The FOS strain measurements provided a sufficient level of resolution to be able to confirm the differences in FE-predicted strain distribution between the cross beams and main girders. They confirmed that the axle loads were more globally distributed along the main girders compared with the more localised strain response experienced by the cross beams. As part of future work, it is hypothesised that the installed monitoring system can be used as a fatigue assessment tool.

(6) The measured strain response along two transverse cross beams, each with different end connection details, located near the midspan of the bridge, were compared with the FE-predicted results. The cross beam with moment end connections experienced a very similar strain response to the cross beam with pinned end connections. This behaviour may stem from the compositely connected reinforced concrete bridge deck slab which may help to redistribute much of the vertical loading carried by the cross beams.

Overall, the installed FOS network proved to be robust and capable of capturing the in-service strain response of the primary structural bridge elements in great detail. The results obtained in this study can be used to not only gain a better understanding of the in-service performance but also for improving both the design and structural evaluation methods of such bridges.

Acknowledgements

The authors gratefully acknowledge the EPSRC and Innovate UK for funding this research through the Centre for Smart Infrastructure (CSIC) Innovation and Knowledge Centre (EPSRC grant reference number EP/L010917/1); the on-site assistance of Jason Shardelow of CSIC; James Oliver, Matthew Timmis, Brad Stanaway and Phil Holland of Laing O'Rourke; Ruth Platt and Mike Henwood of Atkins; and Robert Dean of Network Rail for providing their invaluable support for this project. Data related to this publication is available at the University of Cambridge data repository.

References

BS 5400:Part 3 (2000): *Design of steel bridges*. British Standards Institution, London.

BS EN 1991-2 (2003): *Eurocode 1: Actions on structures - Part 2: Traffic loads on bridges.*

Butler, L.J., Gibbons, N., Middleton, C.R, and Elshafie M.Z.E.B. (2016). "Integrated Fibre-Optic Sensor Networks as Tools for Monitoring Strain Development in Bridges during Construction." *19th IABSE Congress Stockholm*.

Butler, L.J., Lin, W., Xu, J., Gibbons, N., Elshafie, M.Z.E.B. and Middleton, C.R. (2018). Monitoring, modelling and assessment of a self-sensing railway bridge during construction. *Journal of Bridge Engineering, ASCE*. Article in-press.

DIANA 9.4.4. [Computer software] DIANA FEA BV, Delft, Netherlands.

Hendy, C.R., and Jones, R.P. (2011). "Lateral buckling of steel plate girders for bridges with flexible lateral restraints or torsional restraints", *Workshop on Euro-code 4-2, Composite Bridges*. Stockholm, Sweden.

Kaliyaperumal, G., Imam, B., and Righiniotis, T.(2011). "Advanced dynamic finite element analysis of a skew steel railway bridge." *Engineering Structures*. Vol. 33,pp.181-190.

Knight, R.P. (1983). "Economical steel plate girder bridge", *National Bridge Conference*.

Kong, X., Ho, S.C.M., Song, G., Cai, C. S. (2017). "Scour Monitoring System Using Fiber Bragg Grating Sensors and Water-Swellable Polymers." *Journal of Bridge Engineering, ASCE*. 04017029.

Kopare, S.D. and Upase, K. S. (2015). Analysis of Plate Girder Bridge for Class-AA Loadings (Tracked Vehicles), *International Journal of Emerging Trends in Science and Technology*, 2(6), 2645-2655.

Kreuzer (2006). "Strain measurement with fibre bragg grating sensors", *White Paper*, HBM GmbH, Darmstadt, Germany.

Li, H., Li, D., and Song, G. (2006). "Recent applications of fiber optic sensors to health monitoring in civil engineering." *Engineering Structures*, 26, pp.1647–1657.

Lin, W., Taniguchi, N., Yoda, T. (2017a). "A Preventive Strengthening Method for Steel Columns: Experimental Study and Numerical Analyses." *Journal of Constructional Steel Research*. 138C (2017) pp. 357-368.

Lin, W., Taniguchi, N., Yoda, T., Hansaka, M., Satake, S., and Sugino, Y. (2017b). "Renovation of Existing Steel Railway Bridges: Field Test and Numerical Simulation." *Advances in Structural Engineering*. pp.1-15.

Lin, W., Yoda, T., Taniguchi, N. (2015). "Effects of bridge accessories in steel-concrete composite railway bridges in service condition." *Journal of Bridge Engineering*, ASCE. 04015050.

Lin, W., Yoda, T., Taniguchi, N., and Hansaka, M. (2013). "Performance of strengthened hybrid structures renovated from old railway steel bridges." *Journal of Constructional Steel Research*. Vol.85, pp. 130-139.

Lin, W., Yoda, T., Taniguchi, N., Satake, S., Kasano, H. (2014). "Preventive maintenance on welded connection joints in aged steel railway bridges" Journal of Constructional Steel Research. Vol.92, pp. 46-54.

Quadrato et al. (2010). "Cross-frame connection details for skewed steel bridges."*Engineering Structures*. FHWA Research Report, Report No. 0-5701-1.

Regier, R., and Hoult, N.A. (2014). "Distributed strain behavior of a reinforced concrete bridge: case study." *Journal of Bridge Engineering, ASCE*. 05014007.

Sakurai, N., Noro, T, Watanabe, H., Tachibana, S., and Mizoguchi, N. (2002). "An analytical study on two-plate-girders skew bridges." *Nippon Steel Technical Report*, No.86.pp. 94-98.

Scarella, A., Salamone, G., Babanajad, G.S.K., Stefano, A.D. (2016). "Dynamicbrillouin scattering–based condition assessment of cables in cable-stayed bridges." Journal of Bridge Engineering, ASCE. 04016130.

Webb, G. T., Vardanega, P. J., Hoult, N. A., Fidler, R. A. (2017). "Analysis of fiber-optic strain-monitoring data from a prestressed concrete bridge." *Journal of Bridge Engineering, ASCE*. 05017002.

Wijesinghe, B. H. M.P., Zacharie, S.A. Mish, K.D.; and Baldwin, J.D. (2013). "Design and development of in situ fatigue sensors for structural health monitoring of highway bridges", *Journal of Bridge Engineering, ASCE*. 18(4): 297-307.

Zakeri, J.A., and Mosayebi, S.A. (2016). "Study of ballast layer stiffness in railway tracks." *Project Report for Delaware Department of Transportation*. *GRAĐEVINAR*,68(4), pp.311–318.

Zarafshan, A., Iranmanesh, A., and Ansari, F. (2012). "Vibration-Based Method and Sensor for Monitoring of Bridge Scour." *Journal of Bridge Engineering, ASCE*. 17(6): 829-838.

Zhou, J., Bennett, C., Matamoros, A., Li, J., Rolfe, S. (2016). *Skewed Steel Bridges: Effect of Cross-Frame Layout on Lateral Flange Bending Stresses*, Report No.: K-TRAN: KU-13-3.

503

Table 1 Train numbering and information

Train No.	Type	Track side	Speed (km/h)	No. of cars
1	1	East	147	4
2			150	4
3		West	160	4
4			162	4
5	2	East	117	4
6			144	4
7			142	4
8			142	4
9		West	128	5
10			136	5
11			160	5
12			133	4

504

505 **Table 2** Maximum strains on main girders

Train direction	Train near east main girder side						Train near west main girder side					
Train No.	1	2	5	6	7	8	3	4	9	10	11	12
ε_{lgt} (με)	-39	-41	-42	-42	-39	-41	-43	-43	-53	-55	-54	-50
ε_{lgb} (με)	28	32	35	33	32	32	40	40	46	48	47	47
ε_{ulgt} (με)	-18	-18	-17	-20	-19	-19	-19	-17	-20	-19	-19	-21
ε_{ulgb} (με)	17	19	18	18	19	19	11	12	13	15	13	14
$\varepsilon_{ulgt}/\varepsilon_{lgt}$	0.46	0.42	0.41	0.48	0.49	0.45	0.44	0.38	0.38	0.35	0.35	0.41
$\varepsilon_{ulgb}/\varepsilon_{lgb}$	0.59	0.59	0.53	0.55	0.58	0.59	0.28	0.30	0.29	0.30	0.28	0.30

506
507
508
509

Fig.1 Click here to download Figure Fig.1.pdf

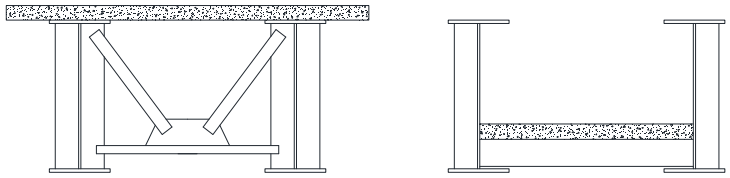

1

2

Fig.2

Click here to download Figure Fig.2.pdf

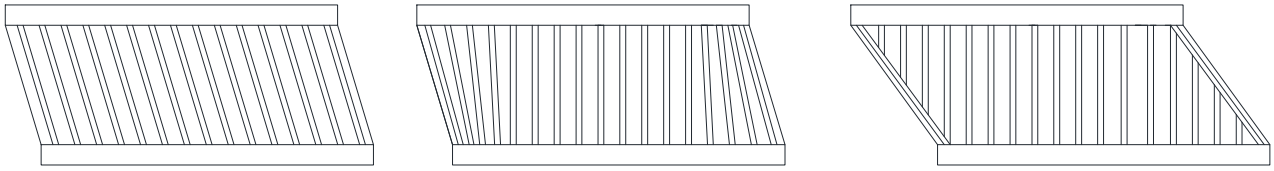

Fig.3 Click here to download Figure Fig.3.pdf

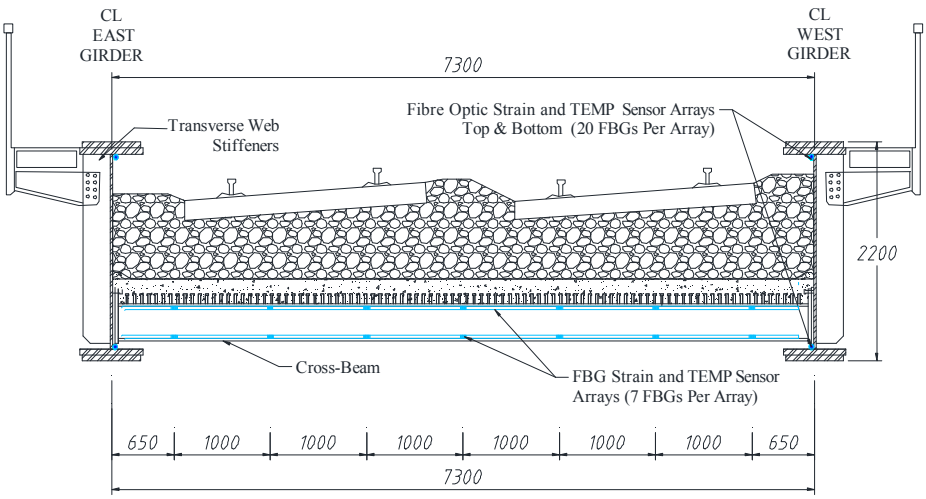

Fig.4 Click here to download Figure Fig.4.pdf

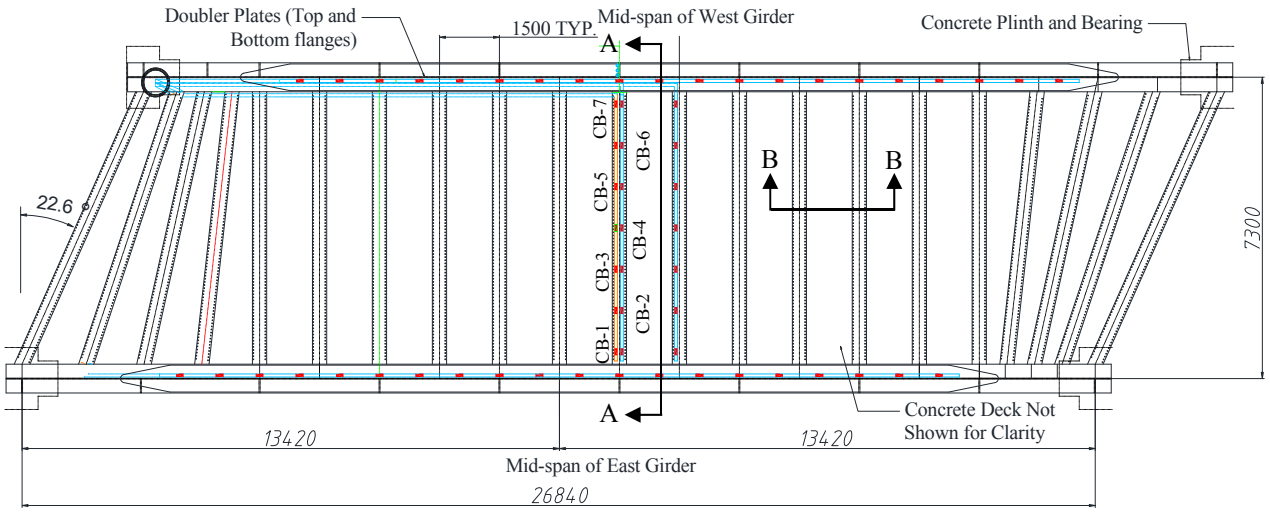

Fig.5

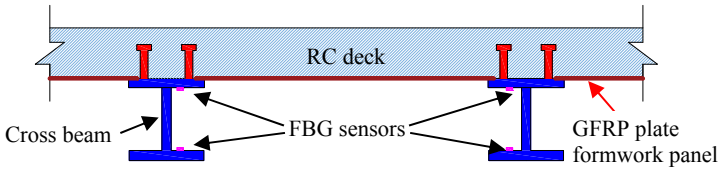

Fig.6 Click here to download Figure Fig.6.pdf

Fig.7 Click here to download Figure Fig.7.pdf

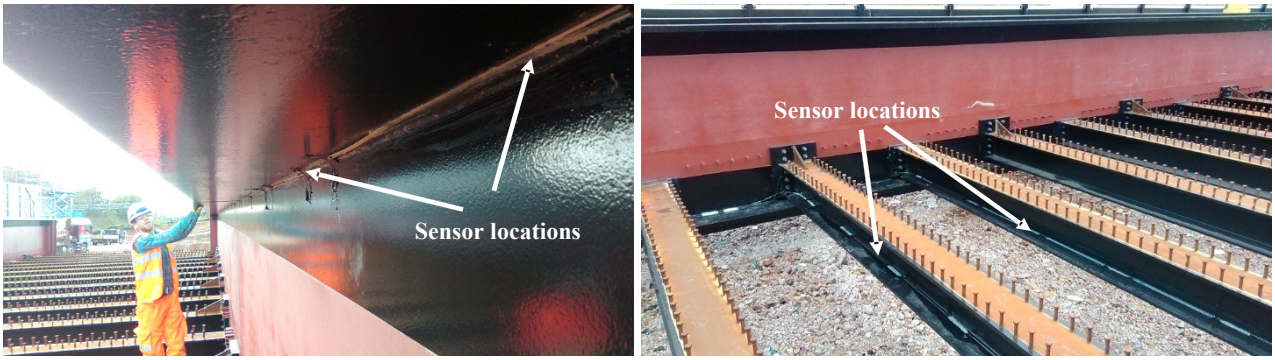

Fig.9

Click here to download Figure Fig.9.pdf

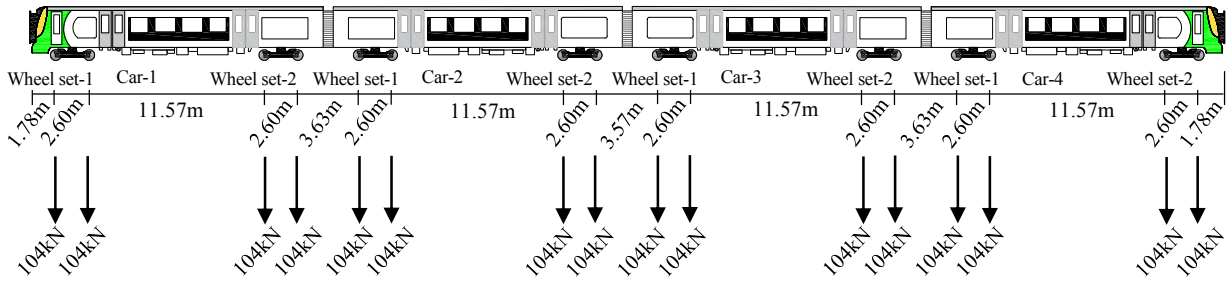

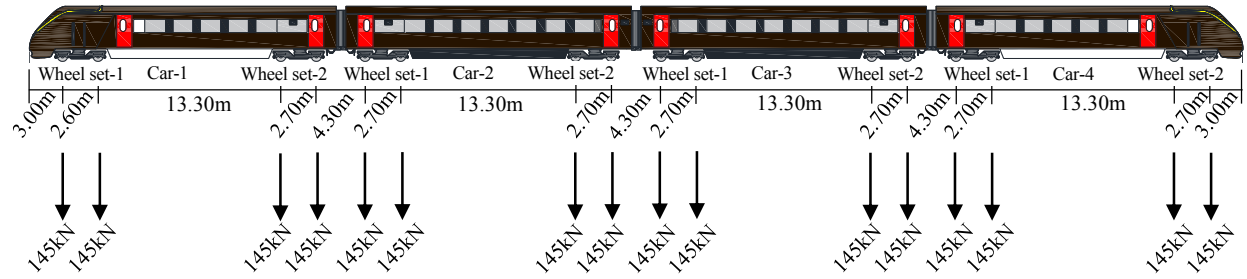

Fig.10

Click here to download Figure Fig.10.pdf

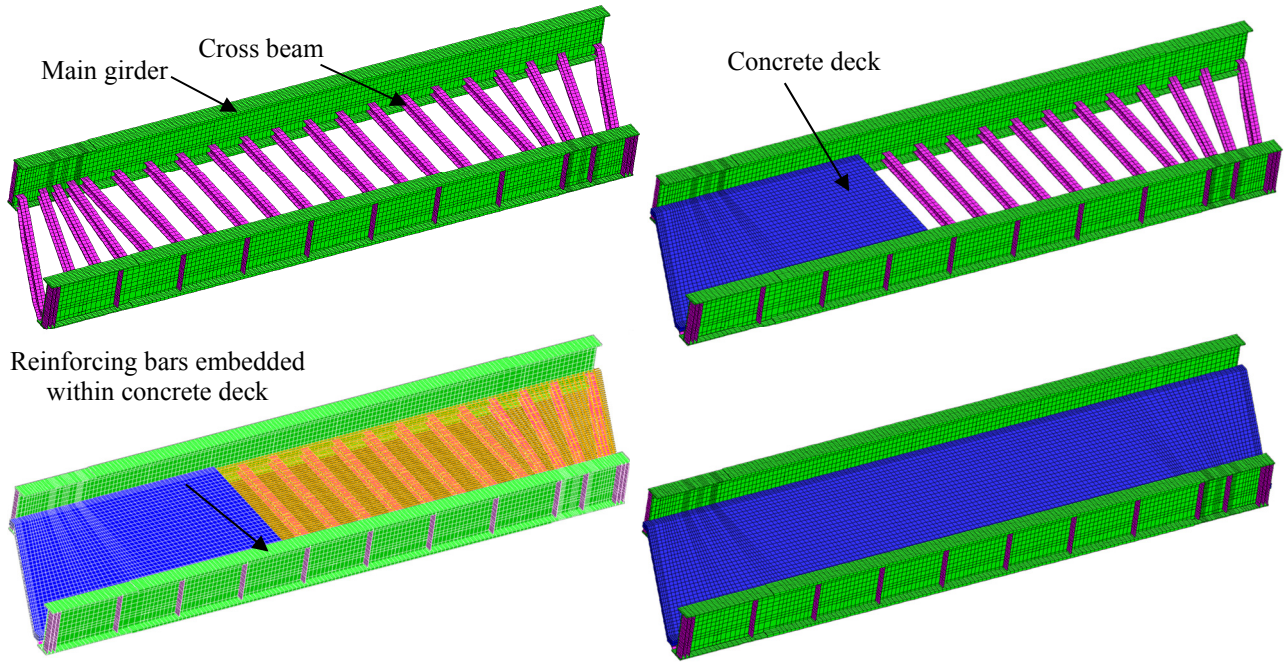

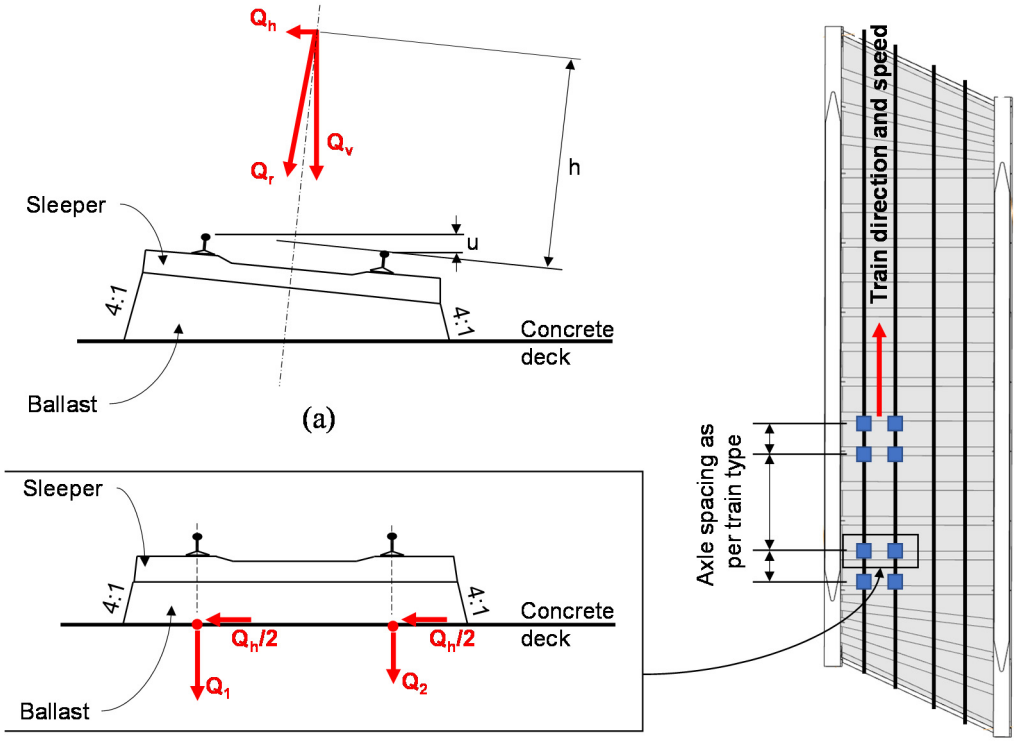

Fig.12

Click here to download Figure Fig.12.pdf

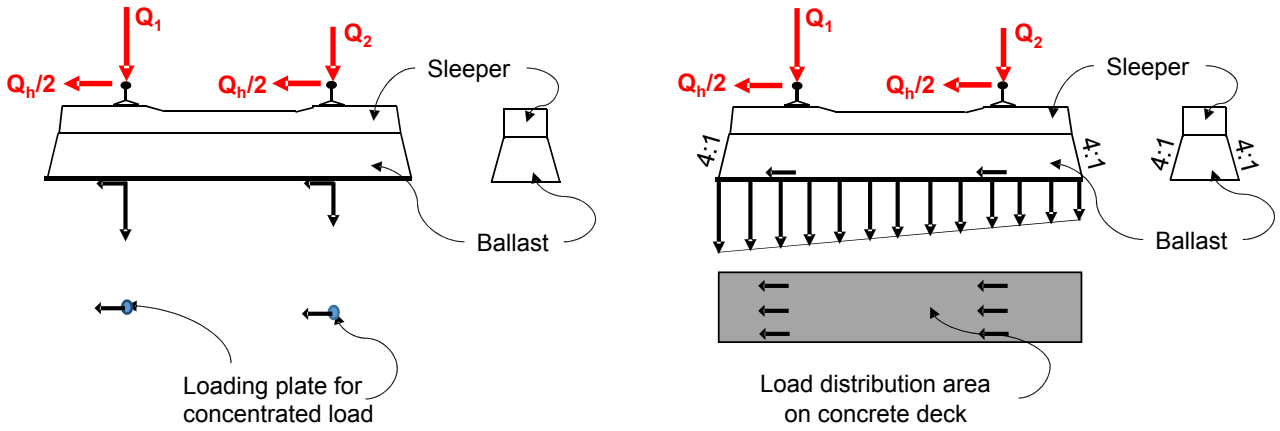

Fig.13 Click here to download Figure Fig.13.pdf

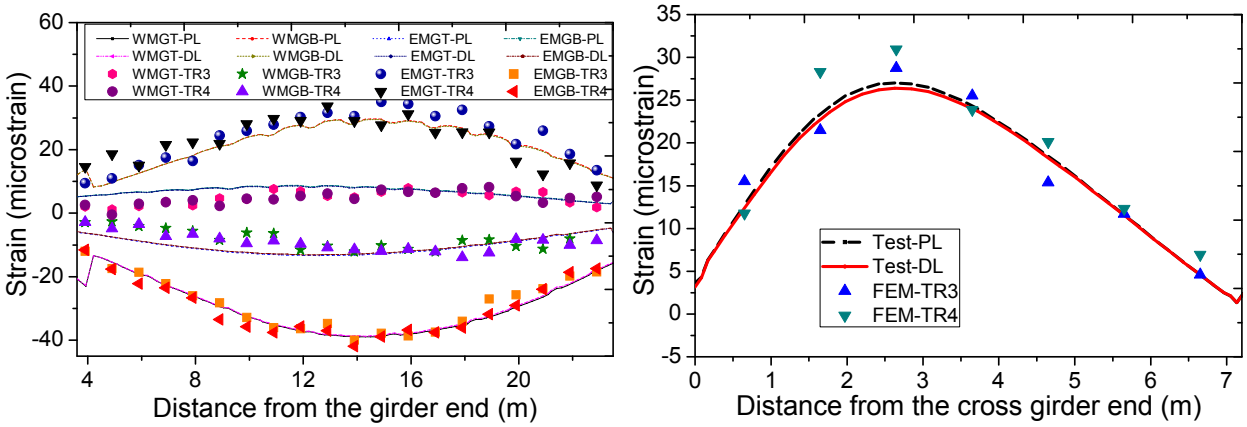

25

26

Fig.14

Click here to download Figure Fig.14.pdf

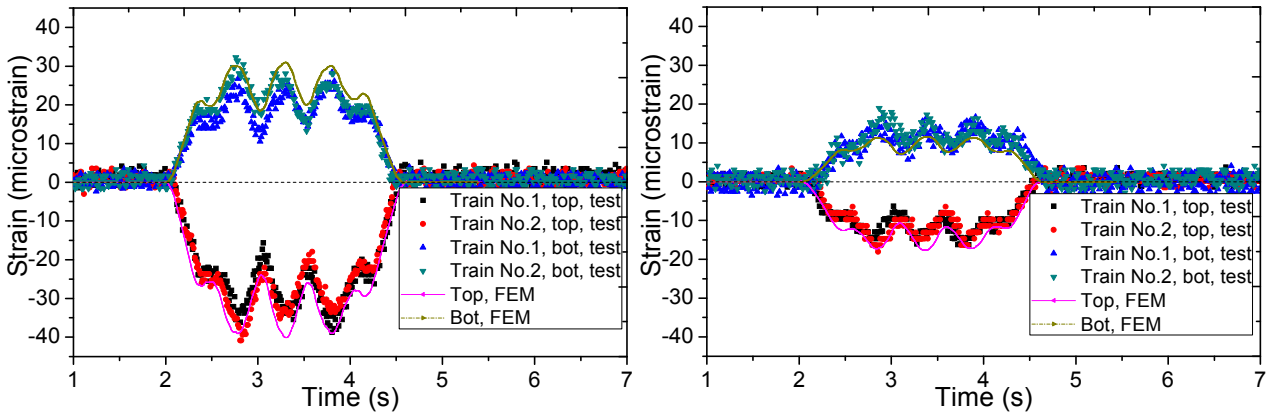

Fig.15

Click here to download Figure Fig.15.pdf

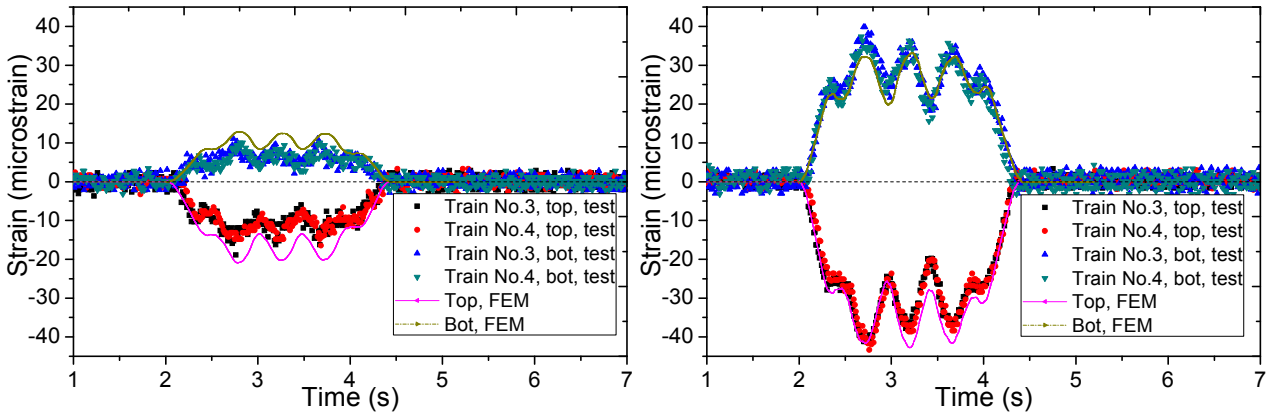

Fig.16

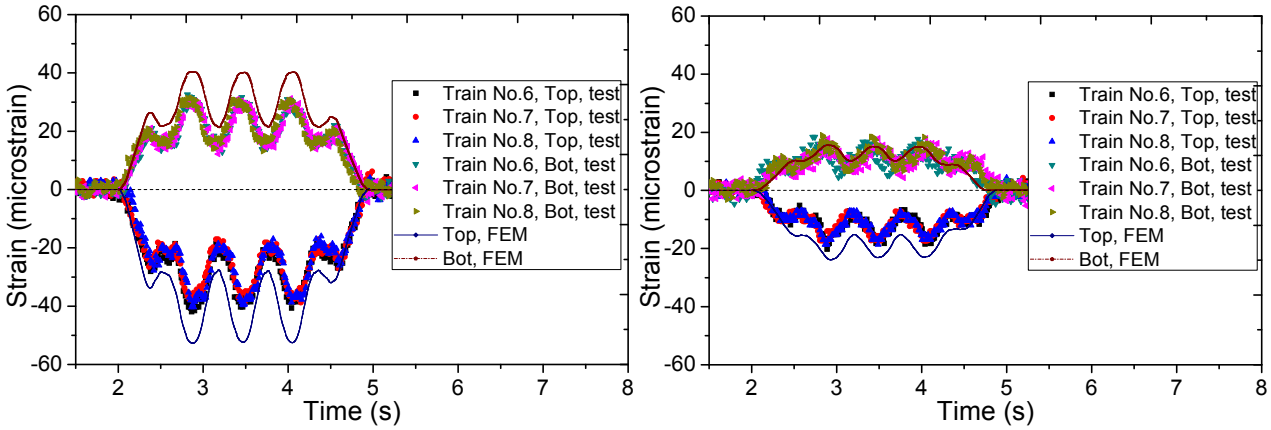

Fig.17

Click here to download Figure Fig.17.pdf

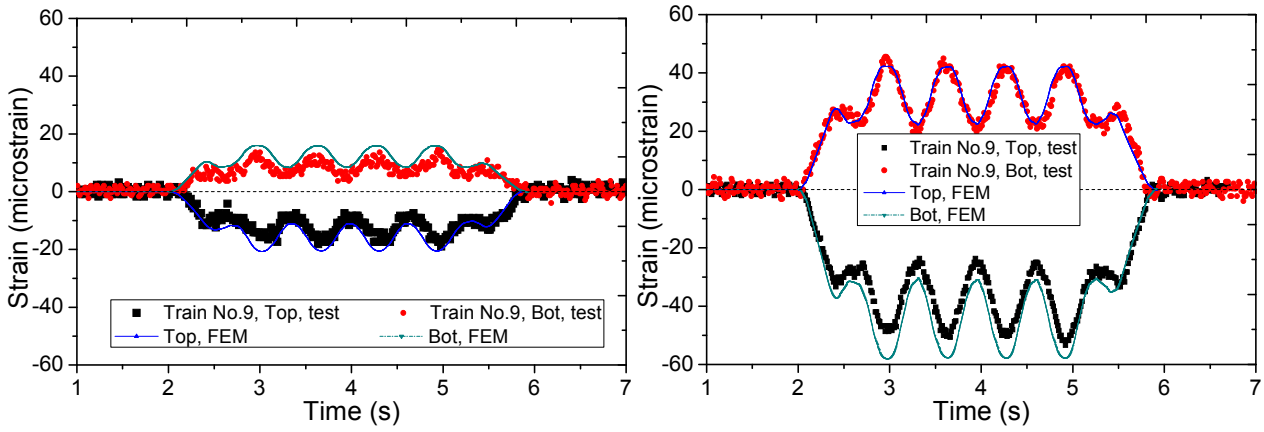

Fig.18

Click here to download Figure Fig.18.pdf

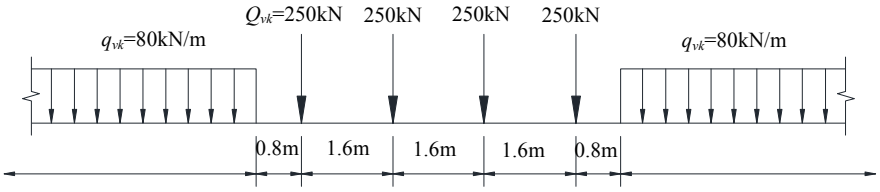

Fig.19

Click here to download Figure Fig.19.pdf

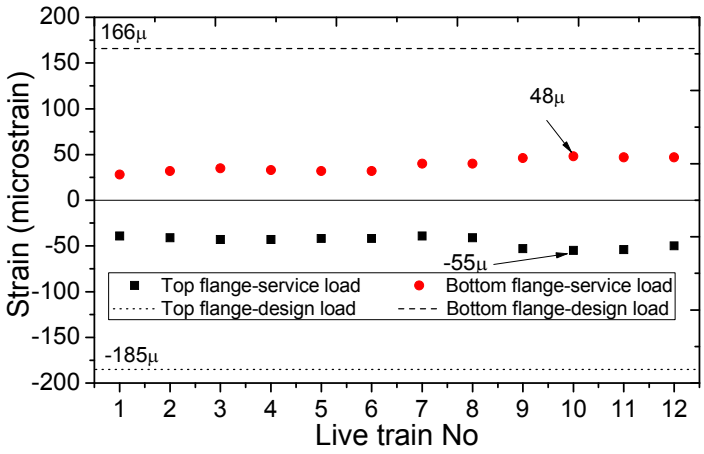

Fig.20

Click here to download Figure Fig.20.pdf

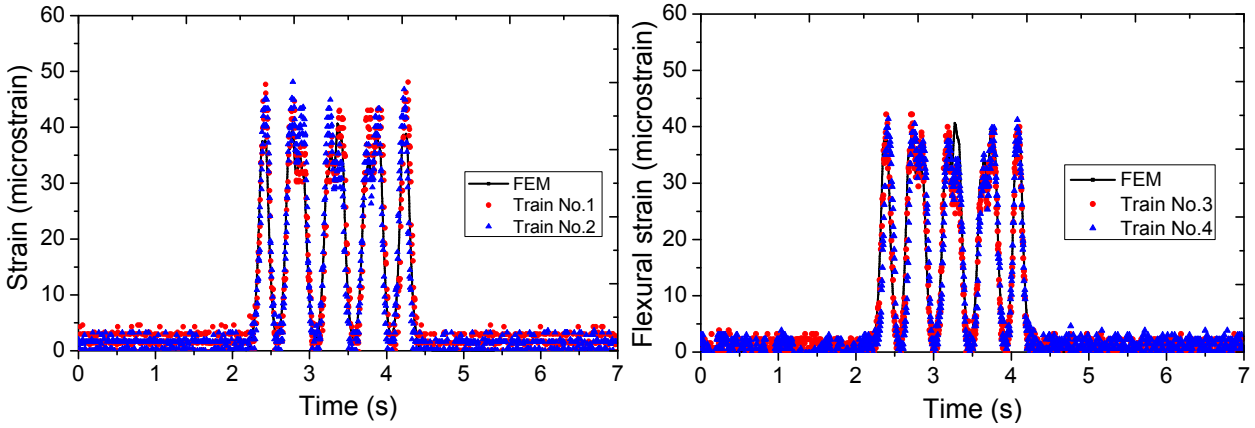

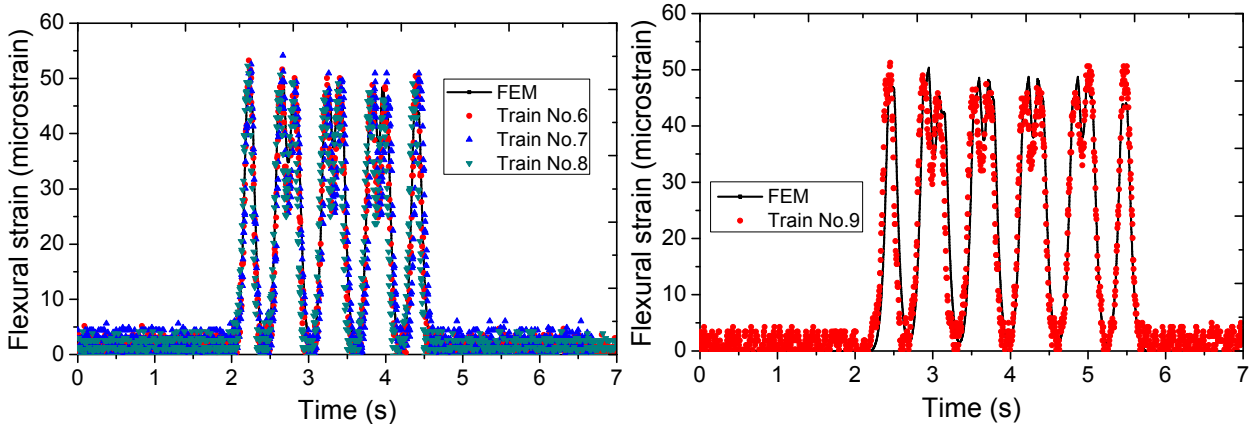

35

36

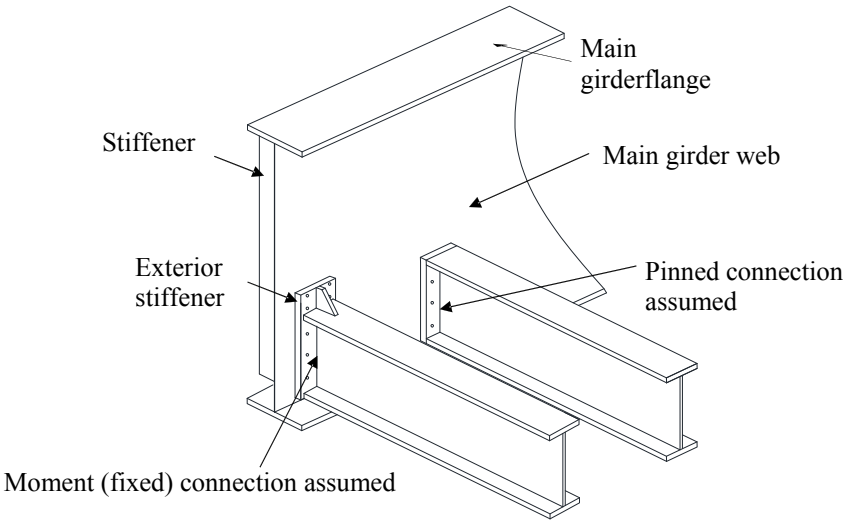

Fig.23

Click here to download Figure Fig.23.pdf